CHARLIS

Results of Magellan 2 primary mirror integration

Steward Observatory Mirror Lab
June 26, 2001

1. Summary

We optimized the support forces for the second Magellan primary mirror in late May and early June, 2001. We chose to control 26 bending modes, and were able to do that with modest correction forces in the range $-31 < \Delta F < 23$ N. The resulting mirror figure is better than we obtained with the mirror on the polishing support. The rms surface error is 22 nm, reducing to 14 nm when astigmatism is subtracted. The image quality is also better than that on the polishing support, with 80% of the light at 500 nm contained in a 0.07″ diameter. Three sets of repeatability measurements demonstrated that this excellent image quality is maintained over several days.

2. Optimization of support forces

The mirror support system was installed in the cell and tested, the 6.5 m mirror was installed, and the system was made available for optical testing and force optimization beginning May 21, 2001. Initial results were limited by seeing (temperature gradients and turbulence in the air) that appeared worse than we had experienced while polishing the mirror. Temperature measurements revealed a thermal instability in the tower, the air handlers making the air at the top colder than the air in the main volume of the lab. The set point for the tower's air handler was adjusted on June 5, and this made a dramatic improvement in seeing. From this point, a single iteration of force adjustment gave the optimized figure presented here, obtained on June 6.

The optimization is done using the mirror's natural bending modes, calculated by BCV using finite-element analysis. Each orthogonal bending mode has a corresponding pattern of actuator forces. Working with Steve Shectman and Paul Schechter, we verified that the force patterns applied by the active support system produce the desired bending modes to high accuracy. We applied force patterns for 5 of the 20 softest modes, and mode 29. Results are given in Table 1 and Figure 1.

In all cases the amplitude of the desired mode is within 20% of the prediction, and within 8% for modes 1, 10, 12 and 13, which have better signal:noise. Leakage into astigmatism is as much as 22% in deflection for the modes with good signal:noise. When one takes into account the stiffness of the modes, this corresponds to less than 1% leakage in force. Even mode 29's 73% leakage in deflection corresponds to less than 0.5% leakage in force. There is negligible crosstalk between complementary modes (the pair of modes with even and odd symmetry about the y axis).

We used 26 modes for the final optimization. The correction forces are all in the range $-31 < \Delta F < 23$ N.

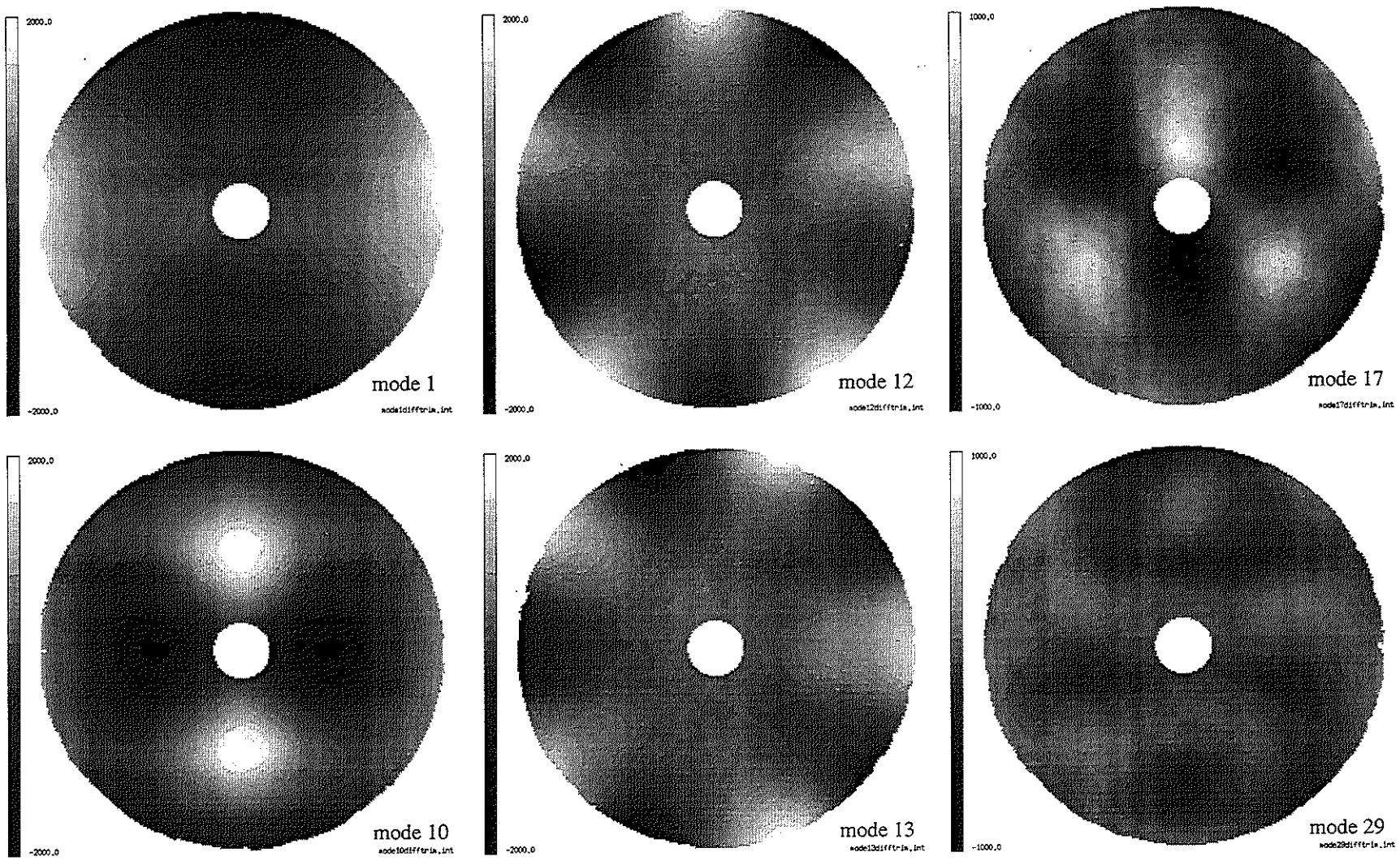

Figure 1. Measured bending modes obtained by applying calculated force sets. Gray-level bars are labelled in nm of wavefront (not surface). Modes 1, 10, 12 and 13 have similar signal:noise. Stiffer modes 17 and especially 29 have less signal but similar noise.

Table 1: Measured modal influence functions

mode	radial zero-crossings	azimuthal symmetry	rms force (N)	predicted rms deflection (nm)	measured rms deflection (nm)	rms in complementary mode (nm)	rms in astigmatism (nm)
1	0	2	2	336	349	11	
10	1	2	60	338	335	0	75
12	0	5	60	296	274	1	27
13	0	5	60	272	267	8	36
17	1	3	60	158	138	4	28
29	1	5	60	64	52	<6	47

3. Figure measurements

Figures 2 and 3 are surface maps and synthetic interference patterns from the measurements made with the optimized forces. All measurements have been corrected for errors in the null lens as determined by the hologram, and for image distortion as determined by the fiducials. A small amount of spherical aberration was subtracted (Zernike coefficient of 9 nm surface, corresponding to 17 parts per million in conic). While spherical aberration is well fit by the bending modes used, we chose not to correct it because the equilibrium value in the telescope will be determined by spacings. The interference patterns are calculated for a wavelength of 633 nm and contain 10 waves of tilt.

The rms surface error is 22 nm including astigmatism, and 14 nm after subtracting astigmatism. Results for the mirror on the polishing support were 150 nm including astigmatism (we made little effort to control it), 20 nm after subtracting astigmatism, and 16 nm after subtracting an additional 3 pairs of Zernike polynomials similar to flexible bending modes. The figure is significantly better on the active support with optimized forces. The figure error on the polishing support was dominated by a high-order astigmatism (mode 10, shown in Figure 1, and its complement) and a high-order spherical aberration. These aberrations were not present consistently over the last few measurements on the polishing support, and may have been due to temperature gradients. The high-order spherical aberration was not present when we optimized the support forces, and the high-order astigmatism, if it was present, was eliminated in the optimization.

4. Encircled energy

We calculated the encircled energy from the map shown in Figure 2. The diffraction calculation covers a 3.6 arcsecond field with 7.2 mas resolution, at a wavelength of 500 nm. Figure 4 shows encircled energy diagrams for the actual mirror and a perfect mirror, in perfect seeing and 0.25 arcsecond seeing. (Seeing is included by convolving the mirror's PSF with that of the atmosphere.) For comparison, Figure 5 shows the same quantities for the mirror on the passive polish-

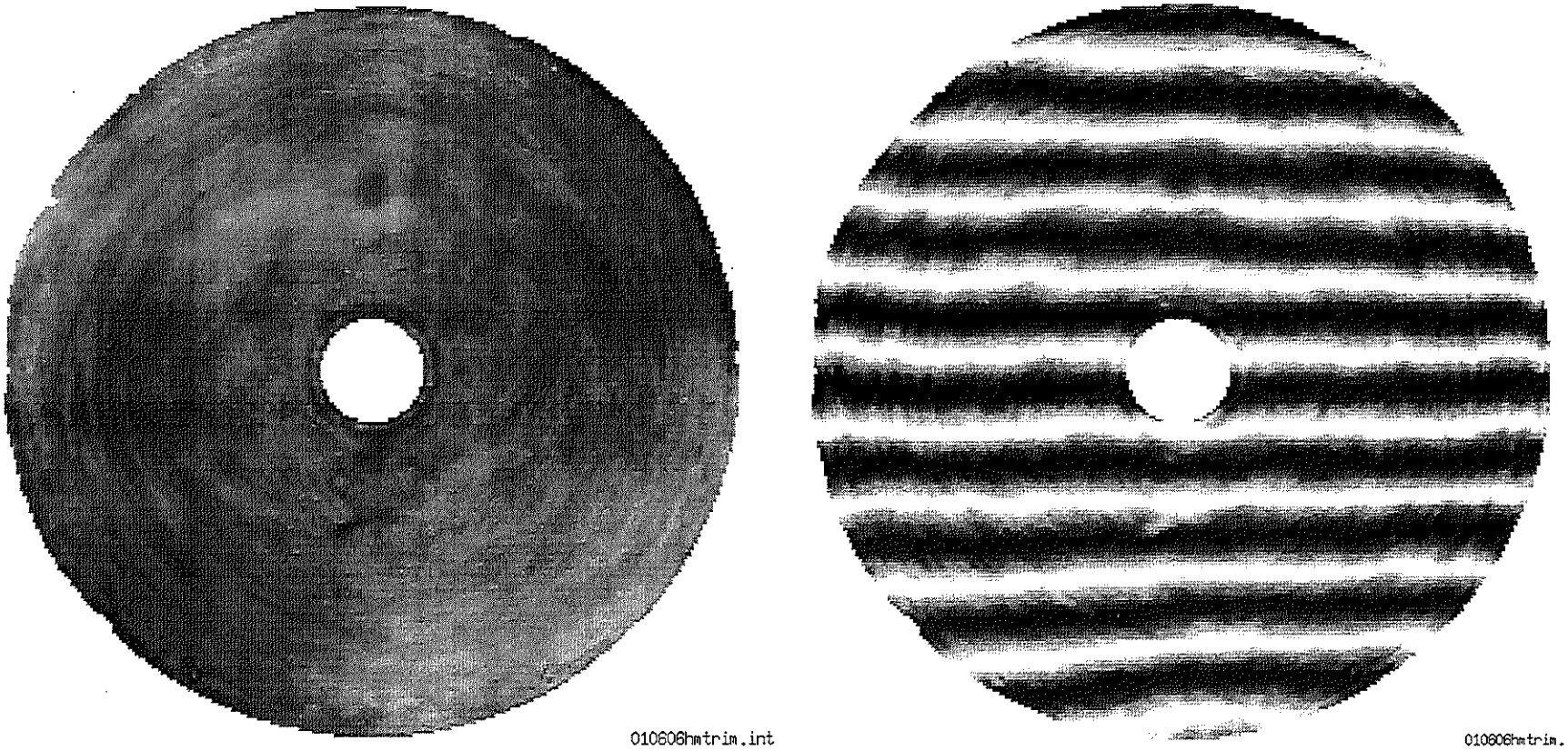

Figure 2. Gray-scale surface map and synthetic interference pattern for the optimized support forces. The gray scale covers ±100 nm of surface. The rms surface error is 22 nm.

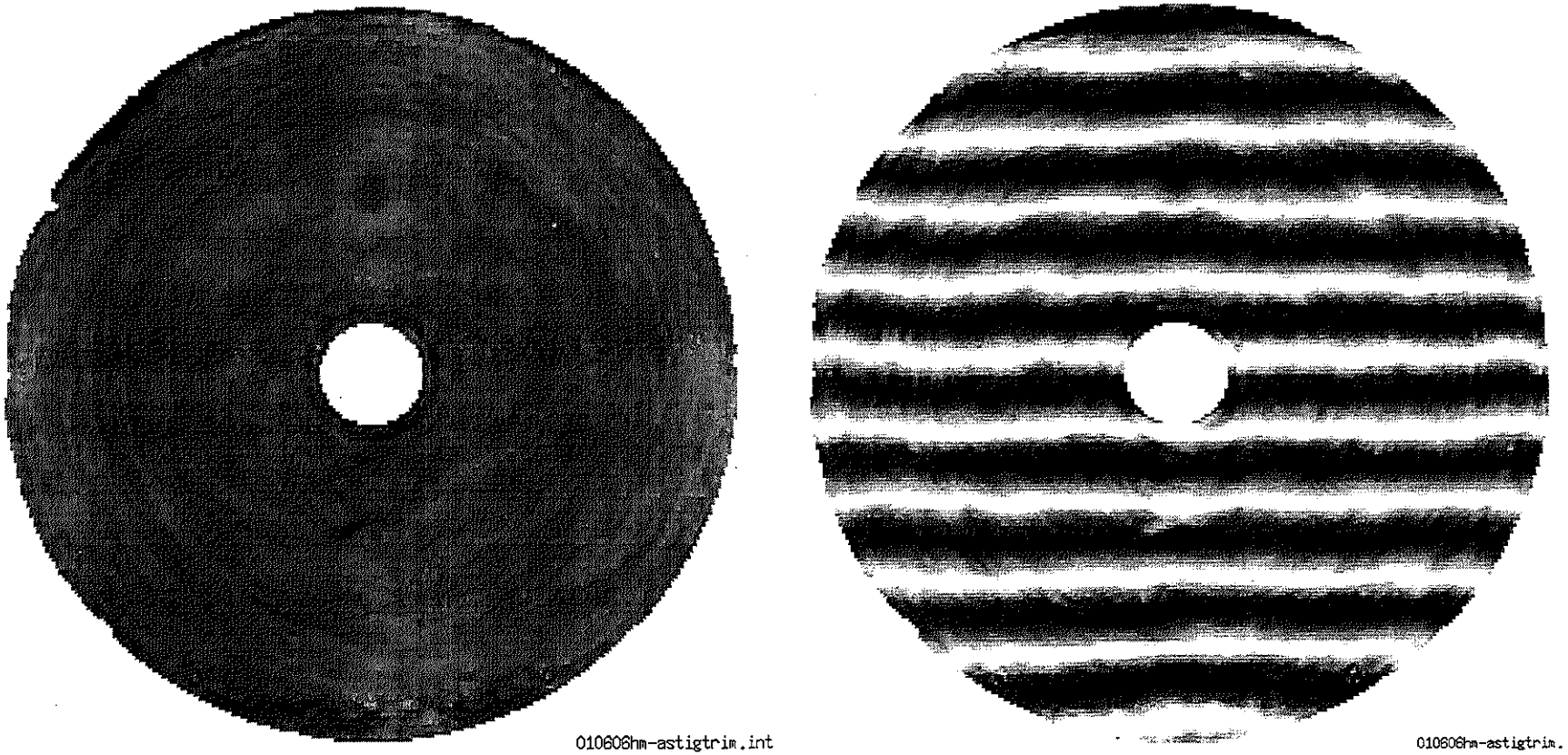

Figure 3. Gray-scale surface map and synthetic interference pattern for the optimized support forces, with astigmatism subtracted. The gray scale covers ±100 nm of surface. The rms surface error is 14 nm.

ing supports, after subtraction of astigmatism. Table 2 gives the diameter containing 80% of the energy for all cases. The mirror on optimized support forces performs better than the mirror on the polishing support.

Table 2: Image diameter containing 80% of the energy at 500 nm

	no seeing	0.25″ seeing
polishing support	0.08″	0.52″
telescope support	0.07″	0.52″
perfect mirror	0.04″	0.49″

5. Figure repeatability

We made three sets of measurements following the optimized results of June 6. In each case the forces were reoptimized, using successively fewer modes. The goal of this exercise was to see how well the lower modes such as astigmatism and trefoil could be controlled when we did not adjust the higher modes. As it turned out, we never improved on the June 6 results, although the final measurement on June 10 was slightly better on small scales and nearly as good on large scales.

Although we applied slightly different forces for the last three measurements, they illustrate the repeatability of the system. If it were perfectly repeatable, the small changes in force would have eliminated the residual astigmatism and other low bending modes obtained on June 6. The presence of these modes in the last three measurements represents non-repeatability, caused by variations in temperature gradients, support forces, or other factors. These measurements therefore give an upper limit on figure changes due to non-repeating forces.

Table 3 gives the surface error obtained in the final four measurements, starting with the best optimized figure of June 6. We also list the number of modes corrected in the current iteration, and the maximum force change in the current iteration. For the June 6 measurement, forces were optimized based on the previous measurement of June 5. For all later measurements, forces were optimized based on the June 6 measurement. (We always used the best measurement to date as the starting point for each iteration.) We give the rms surface error without any synthetic correction, and after subtracting several polynomials similar to the lowest bending modes.

Figure 6 contains encircled energy plots for the final four measurements, starting with June 6 (which is also shown in Figure 4). Table 4 gives the Strehl ratio (central intensity of the point-spread function relative to a perfect mirror) and the diameter θ_{80} containing 80% of the energy, both calculated at 500 nm. The encircled-energy diameters are nearly identical because the figure changes are on such large scales (primarily astigmatism and trefoil) that most of the light

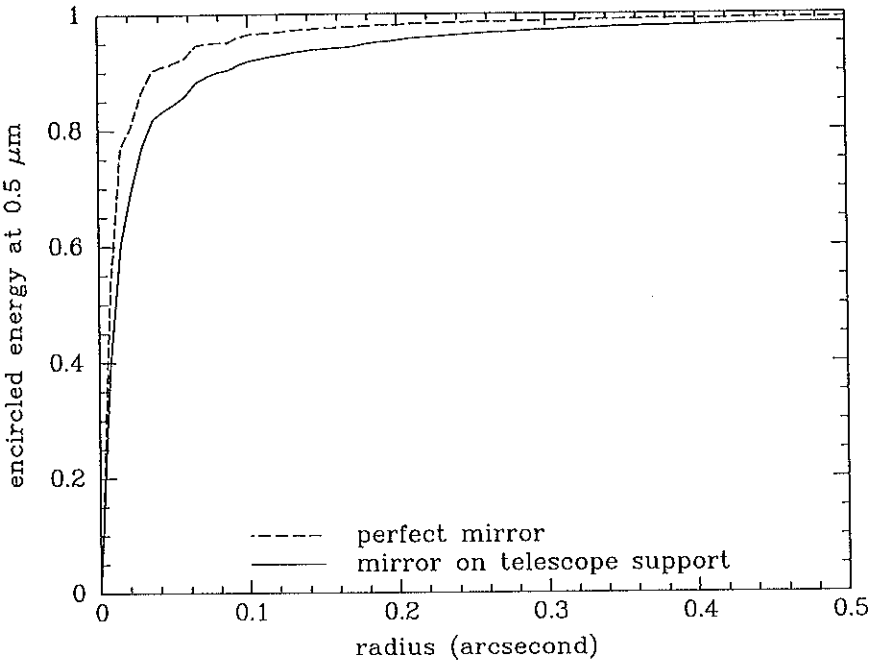

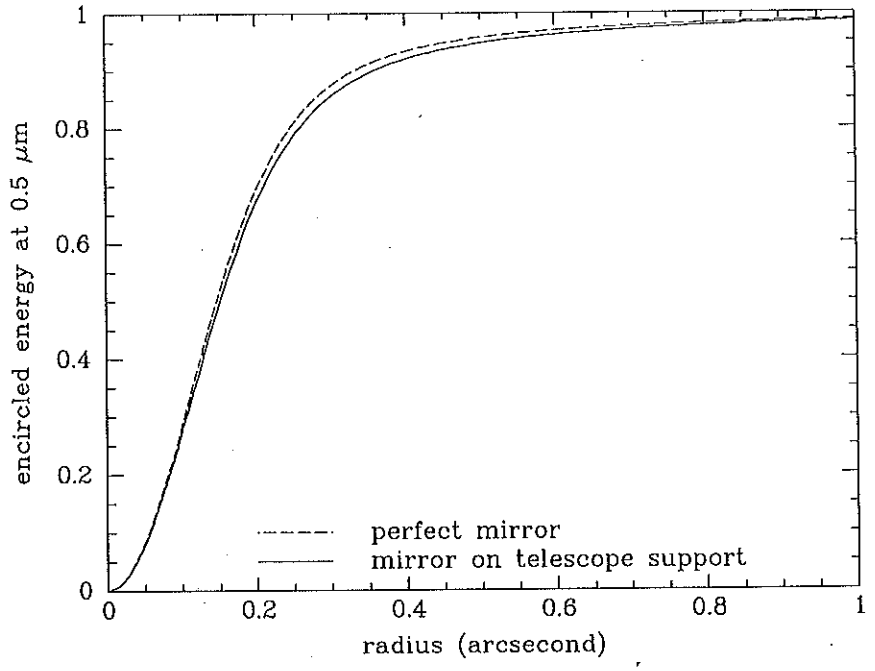

Figure 4. Encircled energy diagram for the mirror of Figure 2 and a perfect mirror. Top: in perfect seeing. Bottom: in 0.25 arcsecond (FWHM) seeing.

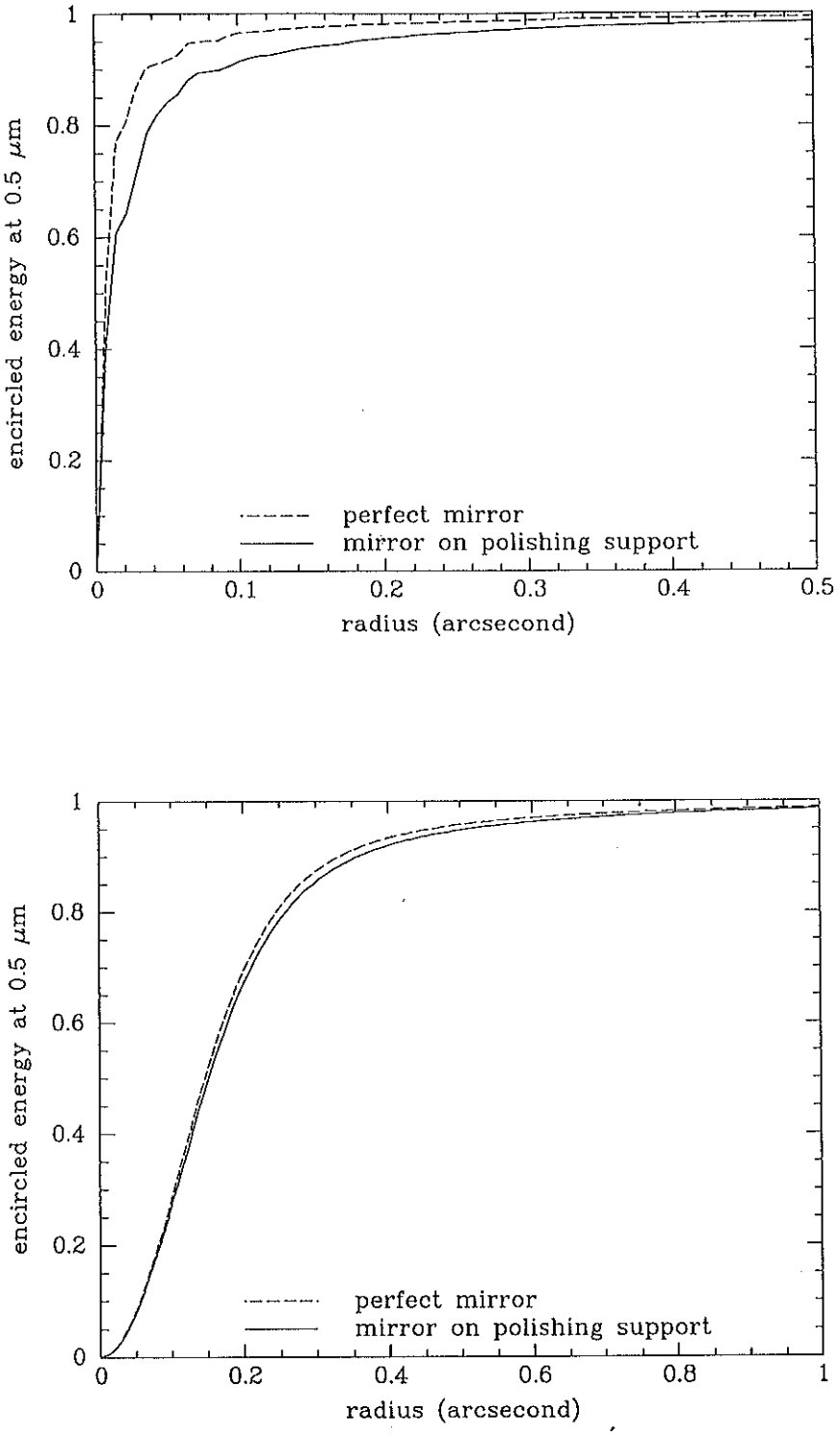

Figure 5. Encircled energy diagram for the mirror on the polishing support, with astigmatism subtracted, and a perfect mirror. Top: in perfect seeing. Bottom: in 0.25 arcsecond (FWHM) seeing.

Table 3: Figure repeatability

date	# modes corrected	max force change (N)	uncorrected rms surface error (nm)	astigmatism subtracted (nm)	+ trefoil subtracted (nm)	+ quatrefoil subtracted (nm)
June 6	26	13	22	14	13	12
June 7	20	6	26	15	15	13
June 8	14	5	28	24	16	16
June 10	9	2	24	16	15	13

remains inside a 0.07″ diameter circle. Thus there is very little degradation in image quality due to non-repeatability.

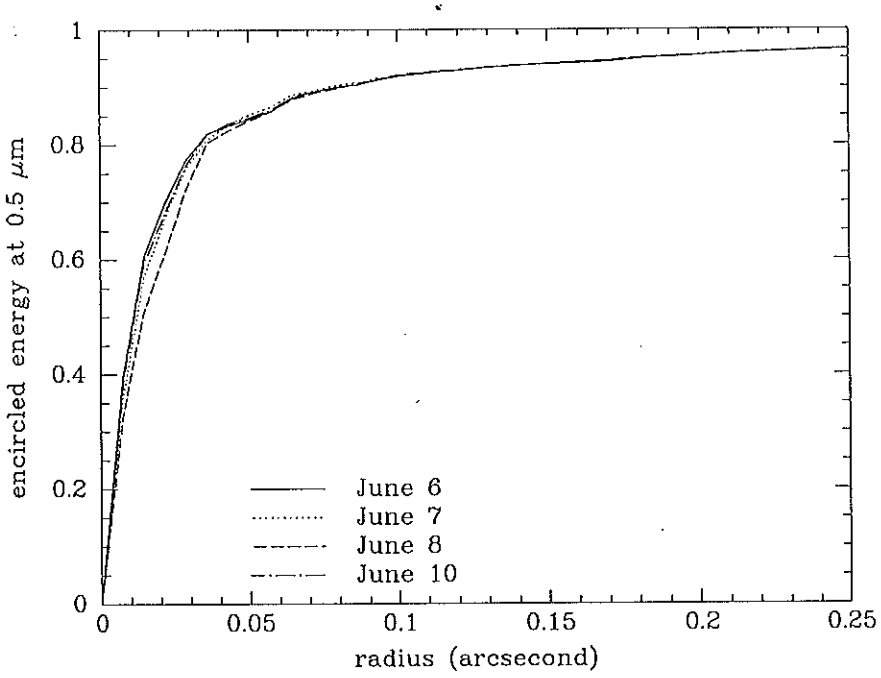

Figure 6. Encircled energy plots for the final four measurements, June 6-10.

6. Optimized forces

The optimized forces, used for the June 6 measurement, are listed in Table 5. These forces are added to the nominal forces from the BCV calculation. The optimized forces will also be transmitted electronically to Magellan staff.

Table 4: Image quality repeatability

date	Strehl ratio	θ_{80}
June 6	0.73	0.07″
June 7	0.64	0.07″
June 8	0.60	0.07″
June 10	0.70	0.07″

Table 5: Optimized forces

actuator ID	force (N)
1	10.4
2	19.9
3	11.8
4	10.2
5	14.1
6	-8.3
7	-1.4
8	3.6
9	0.5
10	-14.3
11	-9.3
12	-2.6
13	-6.0
14	-18.3
15	-14.1
16	-6.2
17	3.2
18	-3.2
19	-13.0
20	-1.8
21	9.1
22	5.0
23	-3.7
24	-3.8
25	16.3
26	7.0
27	-2.9
28	-0.1
29	11.4

Table 5: Optimized forces

actuator ID	force (N)
30	7.0
31	-7.3
32	-3.7
33	7.2
34	1.4
35	3.9
36	-8.7
37	-12.6
38	-0.4
39	3.5
40	-1.2
41	-13.2
42	-13.7
43	1.7
44	9.6
45	2.5
46	-11.9
47	7.6
48	17.7
49	-3.0
50	1.8
51	23.4
52	17.6
101	-2.2
102	1.7
103	6.5
104	-1.5
105	4.1
106	0.1
107	-1.6
108	7.5
109	9.9
110	-7.2
111	3.3
112	14.5
113	0.0
114	-25.3
115	-8.3
116	8.4
117	7.7

Table 5: Optimized forces

actuator ID	force (N)
118	-9.2
119	-17.7
120	-5.2
121	4.5
122	3.5
123	3.4
124	13.9
125	-7.3
126	1.3
127	7.8
128	15.5
129	-9.1
130	-5.4
131	-1.8
132	-3.2
133	3.7
134	-2.8
135	-2.1
136	-0.7
137	-15.2
138	-31.2
139	1.5
140	8.9
141	-0.6
142	-29.3
143	-2.7
144	4.0
145	13.6
146	-1.5
147	-9.7
148	3.5
149	10.4
150	-14.6
151	0.8
152	12.9